Controlling {001} Facet Exposure in TiO Nanoflakes for Enhanced Polysulfide Trapping in Lithium–Sulfur Batteries

*Xiaodong Wu[a, ‡], Weiye Zhang[a, ‡], Jiarui Xue[a], Jiyuan Zhang[a], Ruibin Jiang[a, *], Xuexia He[a], Qi Li[a], Zhibin Lei[a], Zonghuai Liu[a] and Jie Sun[a, *]*

[a]Shaanxi Key Laboratory for Advanced Energy Devices, Shaanxi Engineering Laboratory for Advanced Energy Technology, School of Materials Science and Engineering, Shaanxi Normal University, 620 West Chang'an Street, Xi'an, Shaanxi 710119, China.

*Corresponding authors: Jie Sun, Ruibin Jiang

E-mail address: jiesun@snnu.edu.cn; rbjiang@snnu.edu.cn

1. Dimensionless analysis process on the current-time curves.

Firstly, an analysis is conducted based on the Bewick, Fleischman, and Thirsk (BFT) model[1], which is divided into two-dimensional progressive nucleation (2DP) and two-dimensional instantaneous nucleation (2DI). Among them, 2DP is dominated by lateral surface diffusion, gradually covering un-deposited areas. At low overpotentials, the ion diffusion rate is relatively slow, making it easy to form a continuous thin film. 2DI involves the simultaneous formation of all nuclei, with growth being dominated by the charge transfer rate, which can easily lead to uneven deposition. Furthermore, the Scharifker-Hills (SH) model[2] is also analyzed, including three-dimensional progressive (3DP) nucleation and three-dimensional instantaneous (3DI) nucleation. Among them, 3DP involves the diffusion of ions through the electrolyte to the surface of three-

dimensional nuclei, with growth controlled by the diffusion of the receptor phase. 3DI, on the other hand, involves the simultaneous formation of all nuclei, with growth being controlled by the three-dimensional diffusion field, exhibiting hemispherical diffusion and uniform size. Both of these processes are accompanied by ion diffusion, significantly enhancing the nucleation rate of Li_2S. The theoretical current-time equations for these electrochemical deposition models are as follows[1, 3]:

$$2DI: \frac{I}{I_m} = \left(\frac{t}{t_m}\right) exp\left[-\frac{1}{2}\left(\frac{t^2 - t_m^2}{t_m^2}\right)\right] \quad (S1)$$

$$2DP: \frac{I}{I_m} = \left(\frac{t}{t_m}\right)^2 exp\left[-\frac{2}{3}\left(\frac{t^3 - t_m^3}{t_m^3}\right)\right] \quad (S2)$$

$$3DI: \left(\frac{I}{I_m}\right)^2 = \frac{1.9542}{t/t_m}\left[1 - exp\left(-1.2546\frac{t}{t_m}\right)\right]^2 \quad (S3)$$

$$3DP: \left(\frac{I}{I_m}\right)^2 = \frac{1.2254}{t/t_m}\left[1 - exp\left(-2.3667\frac{t^2}{t_m{}^2}\right)\right]^2 \quad (S4)$$

2. Supplementary Figures and Tables

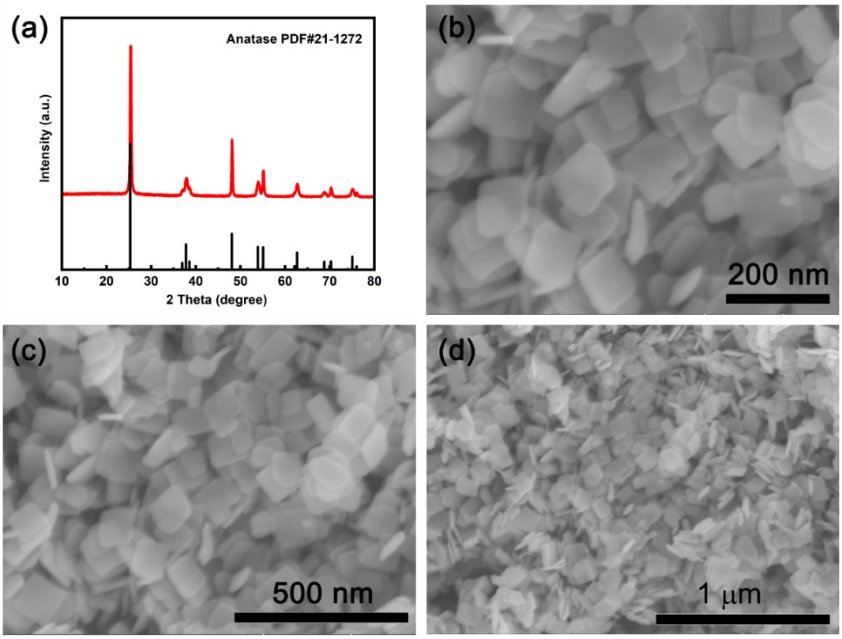

Figure S1 Phase and morphology characterization results of TiO_2-NFs: (a) XRD patterns, (b-d) SEM images with different magnifications.

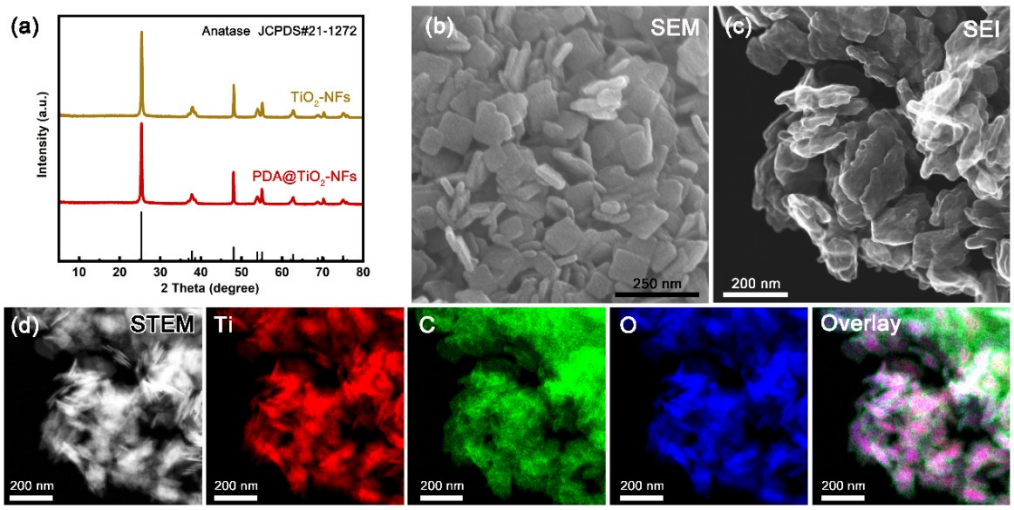

Figure S2 Structure and morphology characterization results of PDA@TiO_2-NFs: (a) XRD Spectrum, (b) SEM images, (c) SEI images, (d) STEM images and EDX mapping images of Ti, O, C elements.

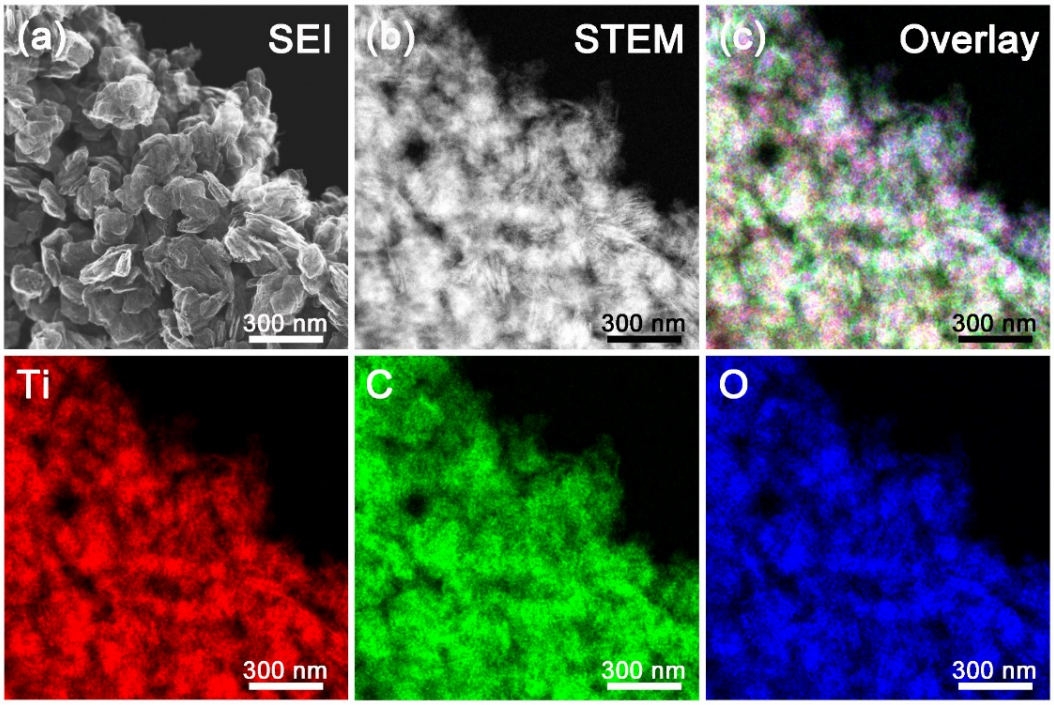

Figure S3 STEM and EDX mapping characterization results of TiO-NFs: (a) SEI; (b) STEM image; (c) EDX mapping of Ti, O, C elements and overlay images.

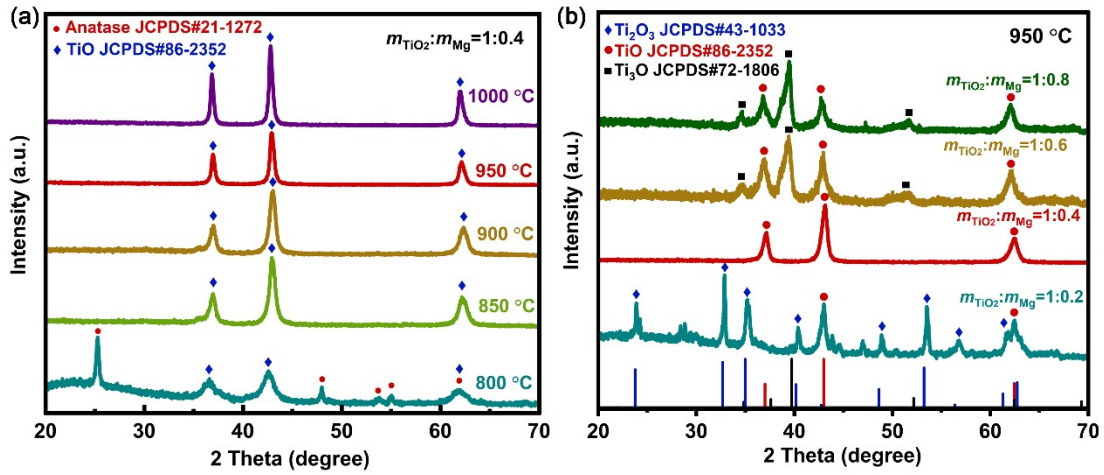

Figure S4 The XRD spectra of the calcinated products without PDA coating after magnesiothermic reduction: (a) XRD spectra of the samples calcinated under different temperatures with the $m_{TiO_2}:m_{Mg} = 1:0.4$; (b) XRD spectra of the samples calcinated at 950 ℃ under different $m_{TiO_2}:m_{Mg}$ ratios.

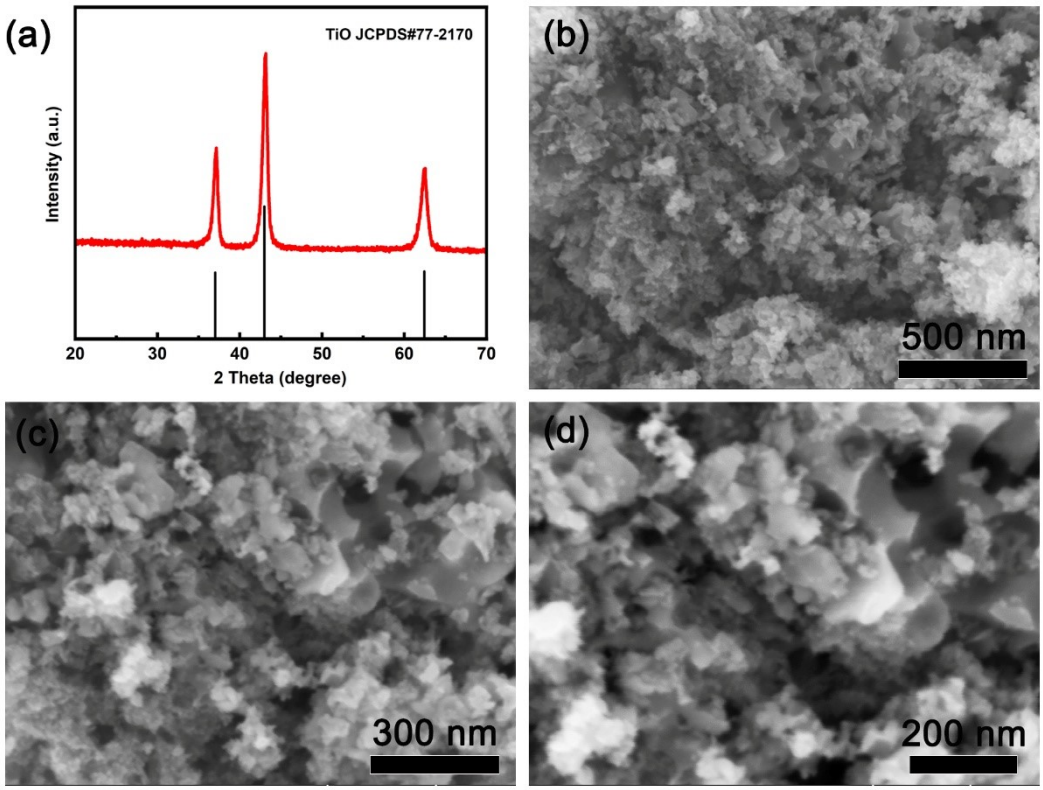

Figure S5 Structure and morphology characterization results of TiO-NPs: (a) XRD patterns; (b-d) SEM images with different magnifications.

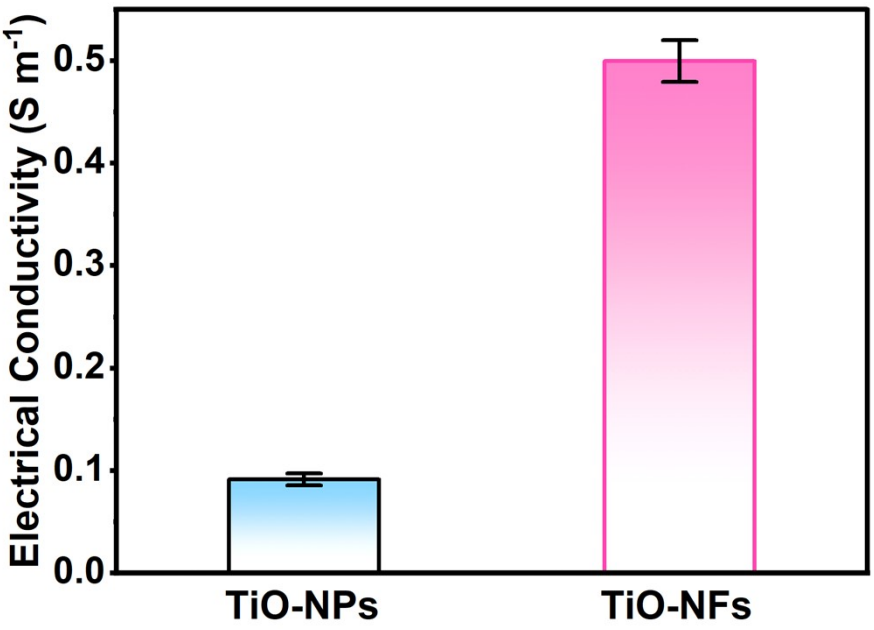

Figure S6 The electrical conductivities of TiO-NPs and TiO-NFs.

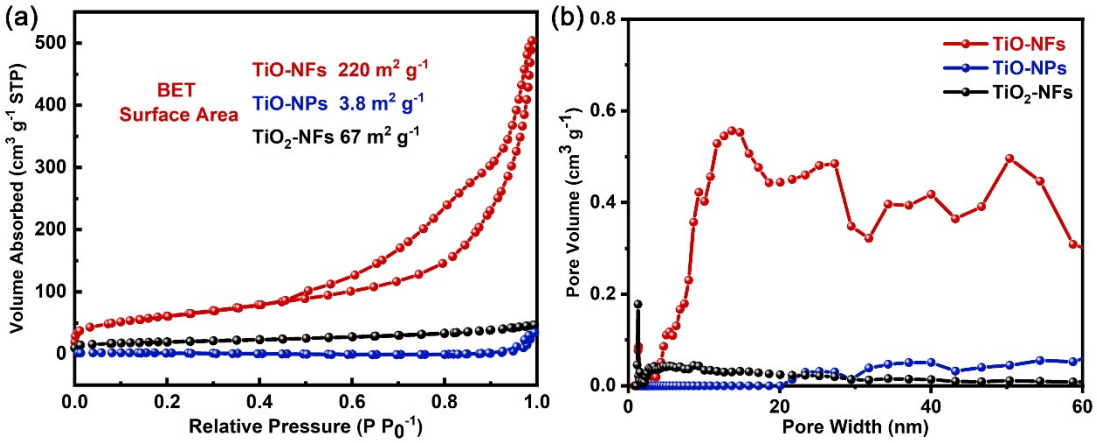

Figure S7 Pore structure characterization results of TiO_2-NFs, TiO-NPs and TiO-NFs: (a) N_2 adsorption-desorption isotherms; (b) pore size distribution curves.

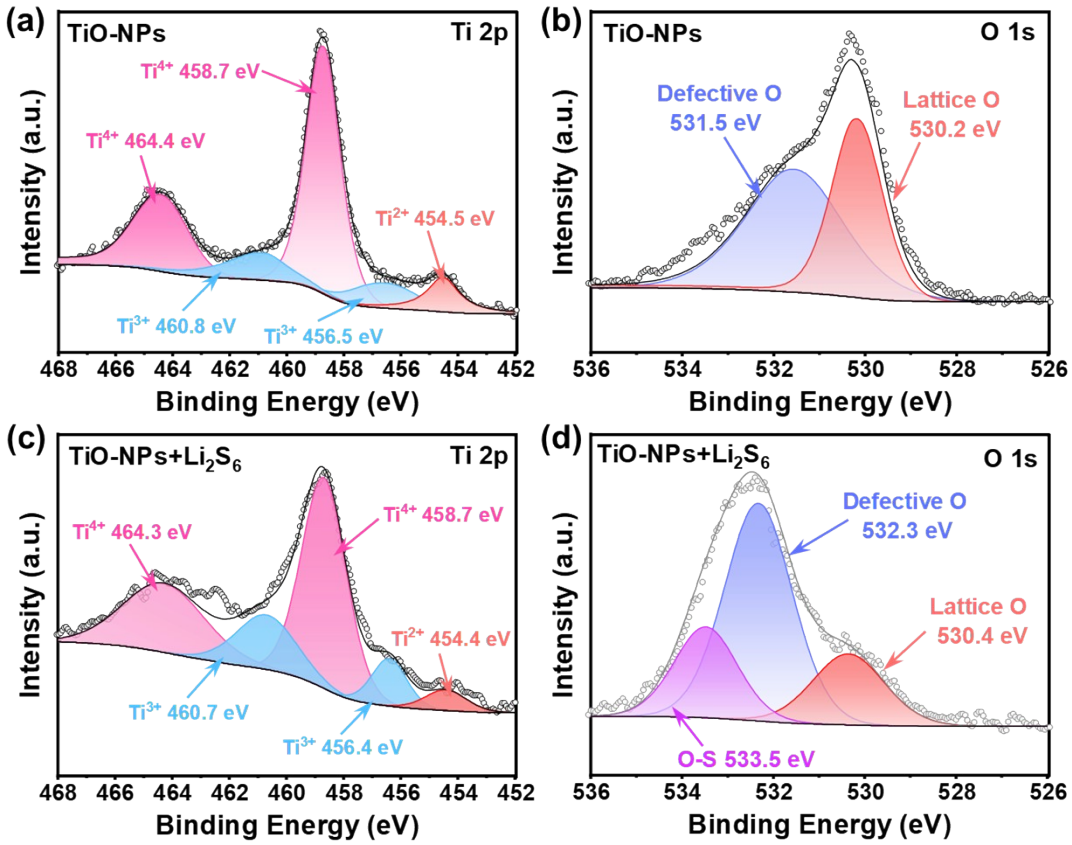

Figure S8 The XPS Ti 2p (a, c) and O 1s (b, d) core level spectra of TiO-NPs before and after Li_2S_6 adsorption.

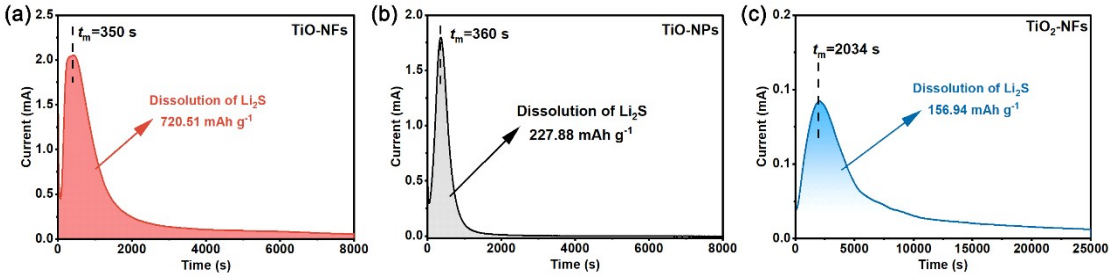

Figure S9 The potentiostatic current-time curves of the cells assembled with TiO-NFs (a), TiO-NPs (b) and TiO_2-NFs (c) as electrodes.

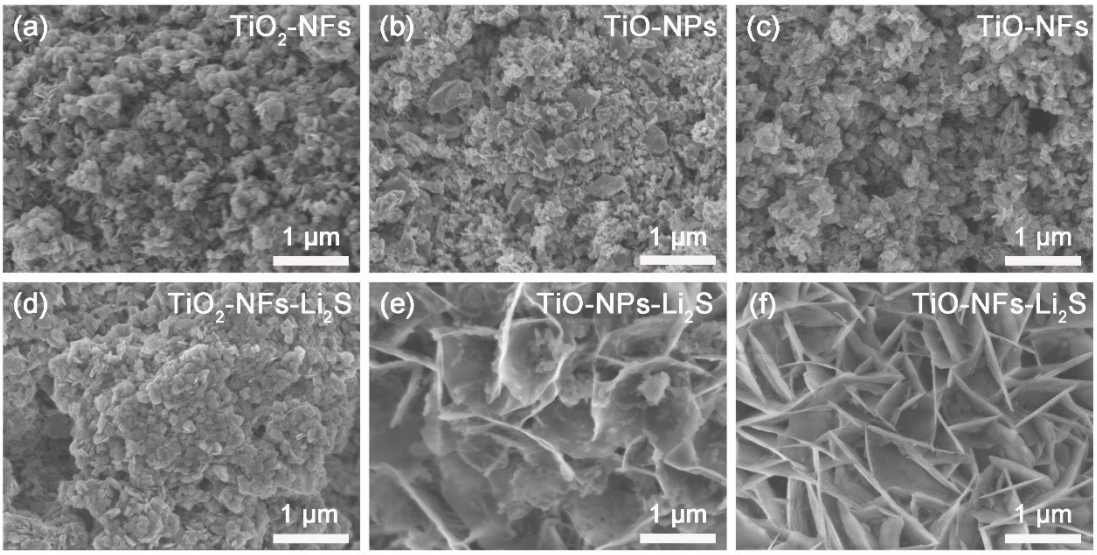

Figure S10 Surface morphological characterization results of TiO-NFs, TiO-NPs and TiO_2-NFs before (a-c) and after Li_2S deposition (d-f).

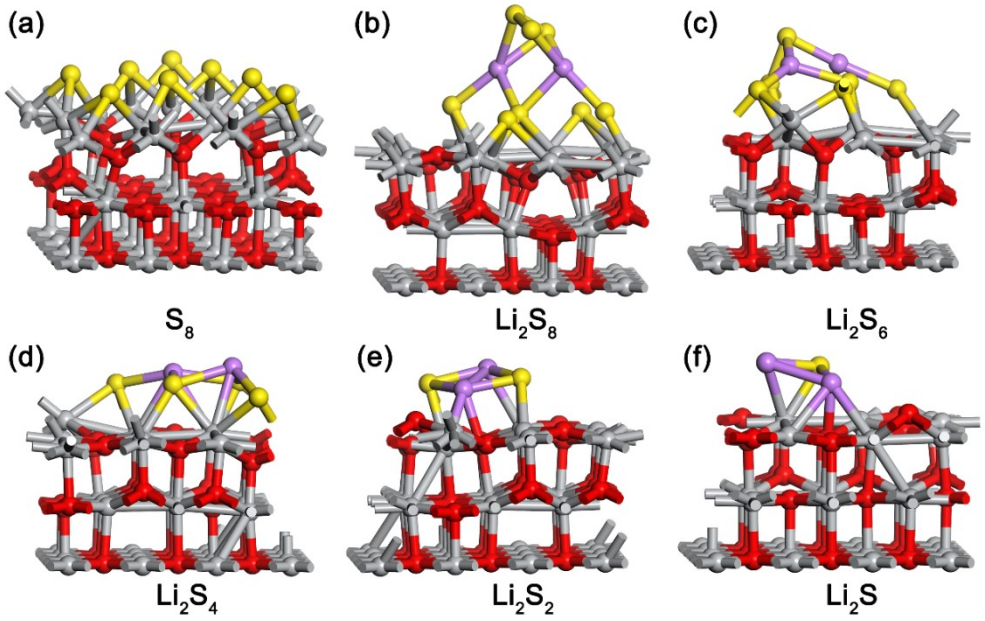

Figure S11 The optimized adsorption configurations of different sulfur species on the surface of TiO (001): (a) S_8; (b) Li_2S_8; (c) Li_2S_6; (d) Li_2S_4; (e) Li_2S_2; (f) Li_2S.

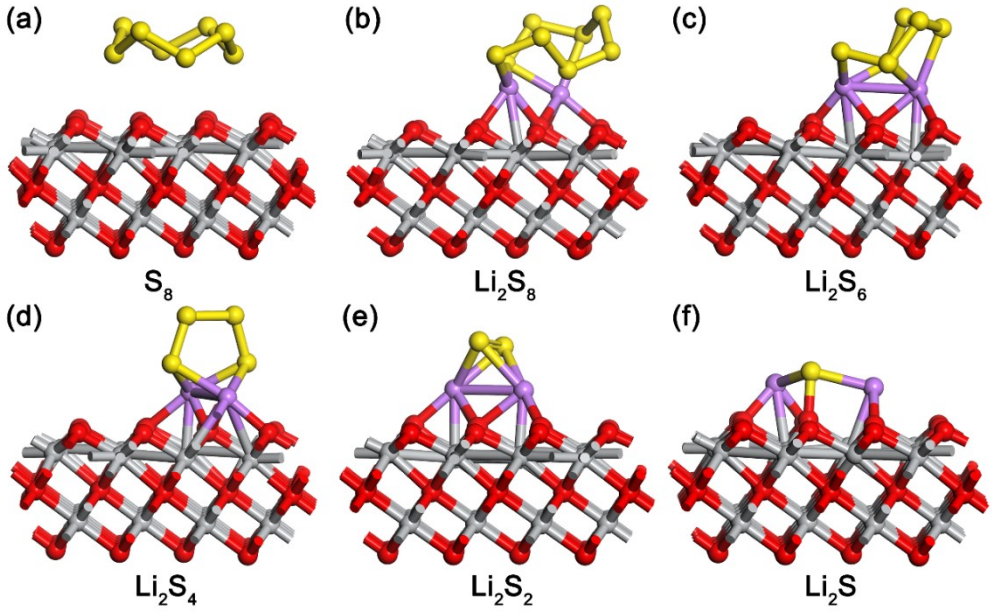

Figure S12 The optimized adsorption configurations of different sulfur species on the surface of TiO (111): (a) S_8; (b) Li_2S_8; (c) Li_2S_6; (d) Li_2S_4; (e) Li_2S_2; (f) Li_2S.

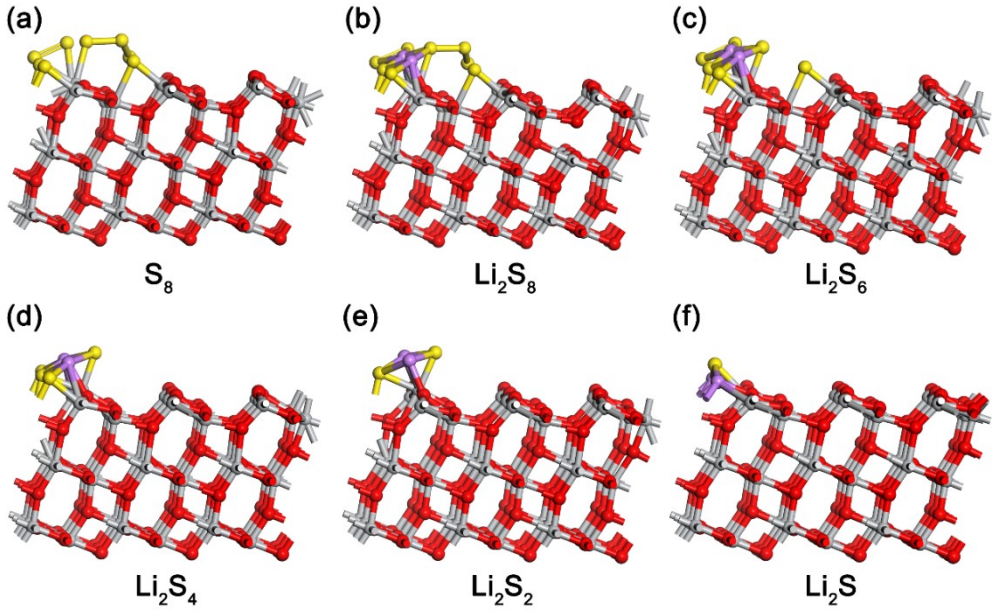

Figure S13 The optimized adsorption configurations of different sulfur species on the surface of TiO_2 (101): (a) S_8; (b) Li_2S_8; (c) Li_2S_6; (d) Li_2S_4; (e) Li_2S_2; (f) Li_2S.

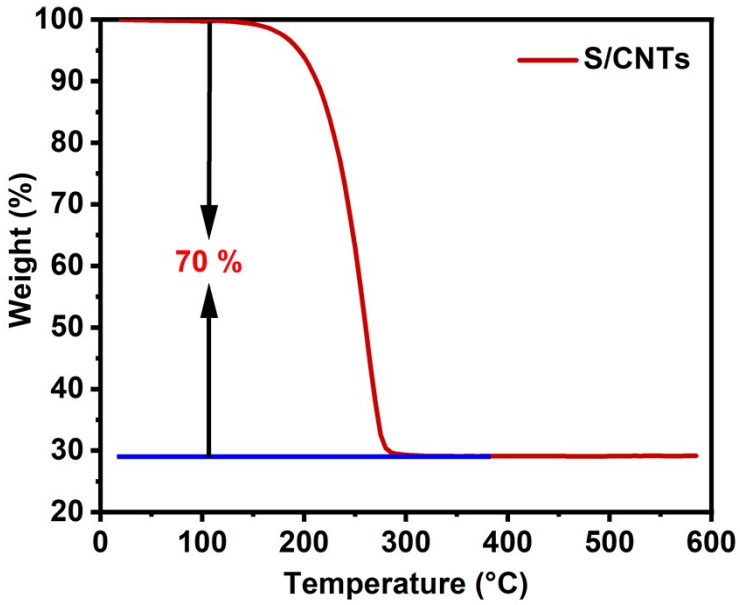

Figure S14 Thermogravimetric analysis results on the S/CNTs composite cathode.

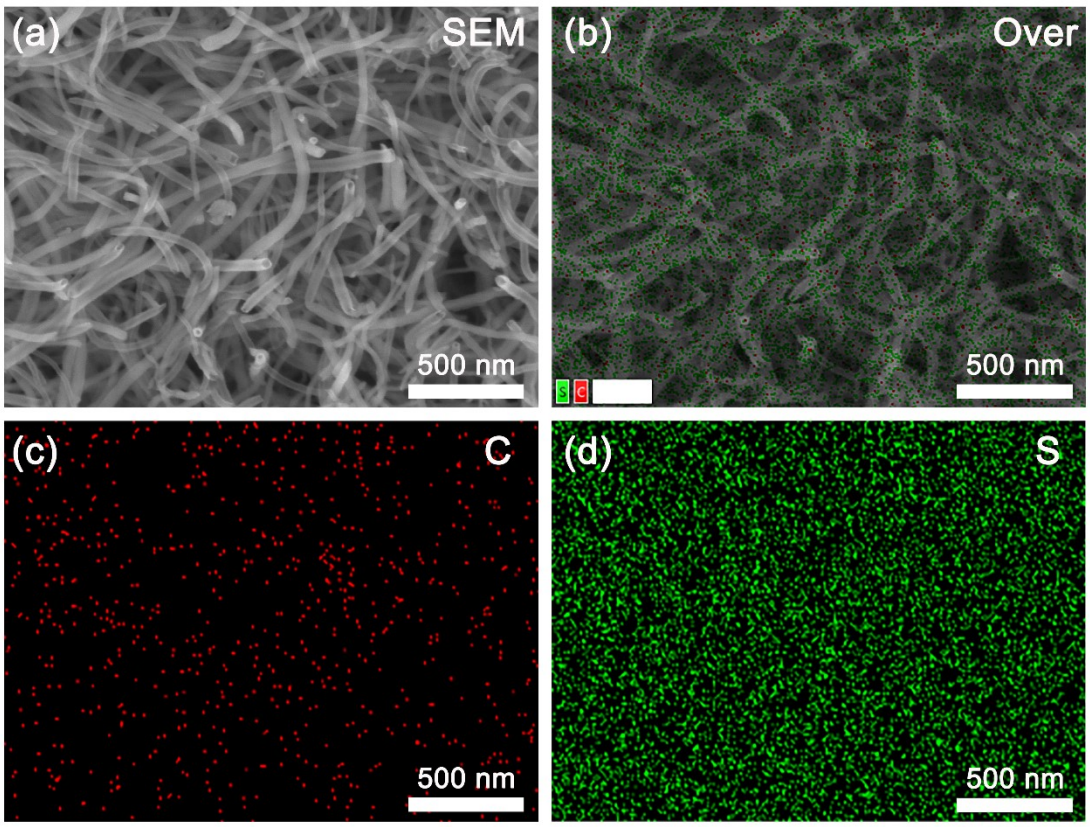

Figure S15 SEM and EDX mapping scan results of the S/CNTs composite cathode.

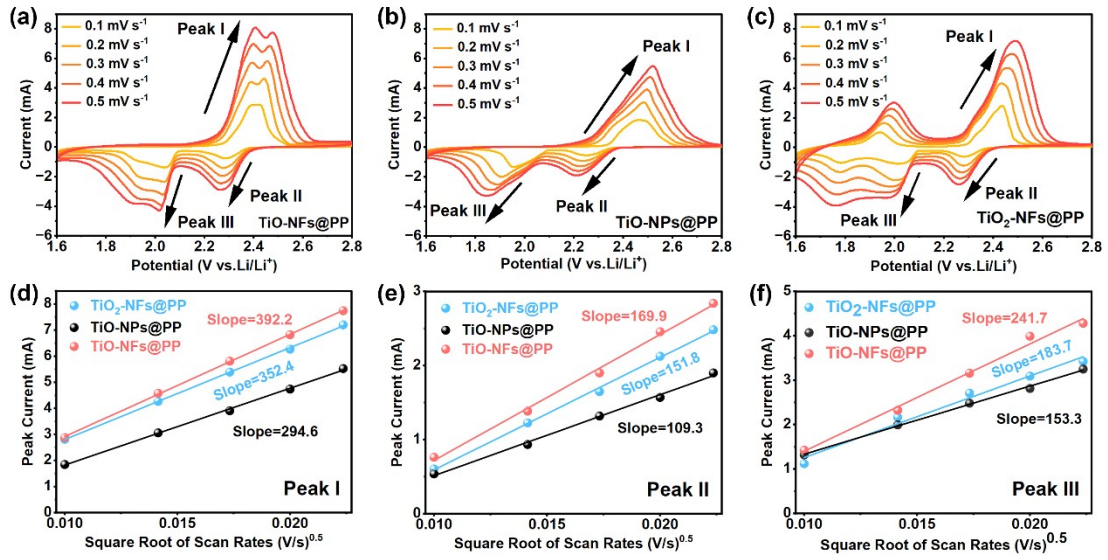

Figure S16 CV curves under different scan rates (a-c) of the cells assembled with different modified separators together with the fitted plots of the 3 redox peaks (d-f).

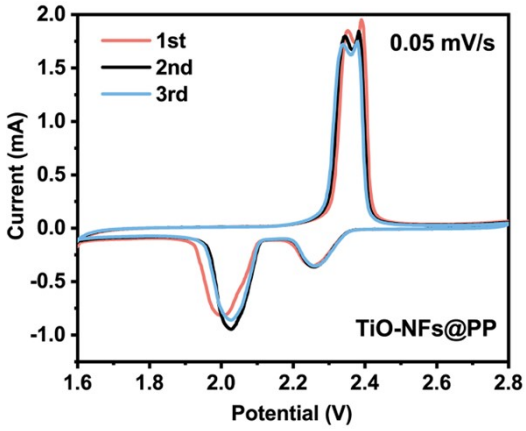

Figure S17 CV curves of the cells under first 3 cycles with TiO-NFs@PP modified separator.

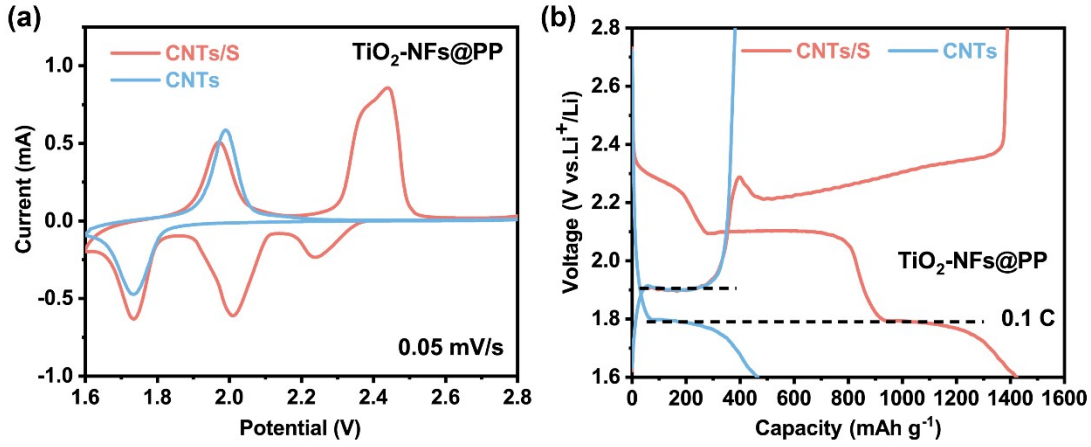

Figure S18 CV curves (a) and the GCD curves (b) of the cells with TiO_2-NFs@PP as the modified separator by using CNTs and CNTs/S as the cathode.

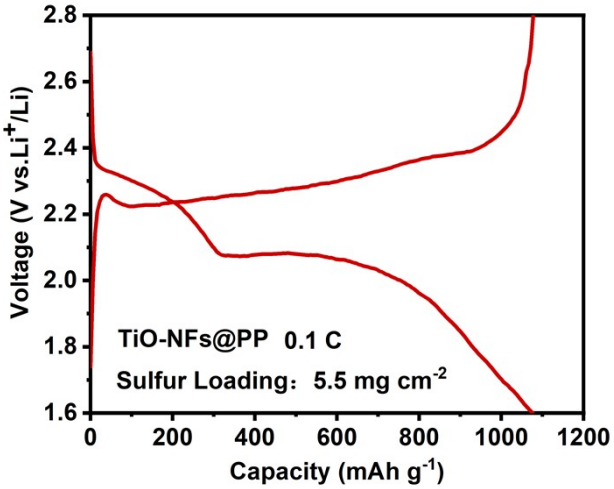

Figure S19 The GCD curves of the cells with TiO-NFs@PP modified separator under the sulfur loading amount of 5.5 mg cm^{-2} at 0.1 C.

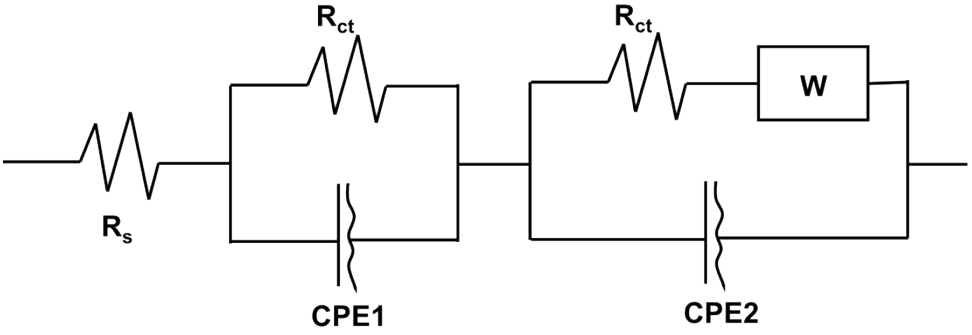

Figure S20 The equivalent circuit used for the fitting of Nyquist plots.

Table S1 The calculation parameters and calculated Li^+ diffusion coefficient of the cells with 3 different modified separators.

Peak		**I**	**II**	**III**
Parameters	n	2	0.5	1.5
	S	0.785	0.785	0.785
	C_0	1.002	1.002	1.002
TiO_2-NFs@PP	$I_p/v^{0.5}$	352.4	151.8	183.7
	D_{Li}^+(cm^2 s^{-1})	3.47×10^{-7}	4.12×10^{-6}	2.23×10^{-7}
TiO-NPs@PP	$I_p/v^{0.5}$	254.6	109.3	153.3
	D_{Li}^+(cm^2 s^{-1})	1.81×10^{-7}	2.14×10^{-6}	1.56×10^{-7}
TiO-NFs@PP	$I_p/v^{0.5}$	392.2	169.9	241.7
	D_{Li}^+(cm^2 s^{-1})	4.29×10^{-7}	5.16×10^{-6}	3.87×10^{-7}

Table S2 Comparison of electrochemical performance of the cells with related titanium oxide based modified separators.

Modification Materials	Sulfur Loading ($mg\ cm^{-2}$)	Current density (C)	Cycle performance ($mAh\ g^{-1}$)	Capacity decay per cycle (%)	Rate performance ($mAh\ g^{-1}$)	References
Flowerlike defective TiO_2	2.5	0.3	100 cycles 1000→545	0.455%	766, 1 C	[4]
TiO_{2-x}@N-doped mesoporous carbon	1.0~1.6	2	500 cycles 908→608	0.067%	694, 4 C	[5]
TiO_2-$Ti_3C_2T_x$ MXene@CNTs	1.3	1	300 cycles 995→867	0.035%	602, 5 C	[6]
TiO_2-graphene	1.4	0.5	300 cycles 914→615	0.109%	NA	[7]
CNTs@TiO_2-B	1.8-2.0	2	1000 cycles 813→472	0.042%	804, 2 C	[8]
TiO-NFs	1.1	1	1000 cycles 1077→339	0.068%	835, 2 C	This work

References

(1) Bewick, A.; Fleischmann, M.; Thirsk, H. Kinetics of the electrocrystallization of thin films of calomel. *Transactions of the Faraday Society* **1962**, *58*, 2200-2216.

(2) Li, Z.; Zhou, Y.; Wang, Y.; Lu, Y.-C. Solvent-Mediated Li2S Electrodeposition: A Critical Manipulator in Lithium–Sulfur Batteries. *Advanced Energy Materials* **2019**, *9* (1), 1802207.

(3) Chu, H.; Noh, H.; Kim, Y.-J.; Yuk, S.; Lee, J.-H.; Lee, J.; Kwack, H.; Kim, Y.; Yang, D.-K.; Kim, H.-T. Achieving three-dimensional lithium sulfide growth in lithium-sulfur batteries using high-donor-number anions. *Nature Communications* **2019**, *10* (1), 188.

(4) Fan, X.; Liu, H.; Wang, H.; Hu, W.; Tian, X.; Pang, L. Understanding the synergistic improving adsorbed and catalytic activity of polysulfide by design of oxygen vacancies and Li+ lithiation/delithiation behavior in Titanium Oxide separator. *Electrochimica Acta* **2024**, *485*, 144142.

(5) Zhou, J.; Sun, S.; Zhou, X.; Rao, X.; Xu, X.; Zhang, Z.; Pan, Z.; Wang, Q.-C.; Wang, Z.; Wu, Y.; et al. Defect engineering enables an advanced separator modification for high-performance lithium-sulfur batteries. *Chemical Engineering Journal* **2024**, *487*, 150574.

(6) Huang, Y.; Chen, Y.; Xu, Q.; Xu, C.; Yang, L.; Jiang, N.; Zhong, J.; Zhao, X.; Yin, S. TiO2-Ti3C2Tx MXene@CNTs hybrids modified polypropylene separator for high-performance lithium-sulfur battery. *Journal of Energy Storage* **2025**, *113*, 115645.

(7) Li, F.; Wei, L.; Wang, M.; Zhu, Y.; Xu, S.; Qiu, X.; Su, C.; Kudashev, S.; Wei, T. An ultralight TiO2-graphene composite layer as separator coating to improve performance of lithium sulfur battery. *Journal of Energy Storage* **2025**, *125*, 116930.

(8) Zhen, M.; Jiang, K.; Guo, S.-Q.; Shen, B.; Liu, H. Suitable lithium polysulfides diffusion and adsorption on CNTs@TiO2-bronze nanosheets surface for high-performance lithium-sulfur batteries. *Nano Research* **2022**, *15* (2), 933-941.